communications biology

A Nature Portfolio journal

https://doi.org/10.1038/s42003-025-08784-4

Demonstration of chemotherapeutic-mediated changes in meningeal lymphatics in vitro, ex vivo, and in vivo

L. Monet Roberts[1,4], Jennifer H. Hammel[1,2,4], Peng Jin[2], Jessica J. Cunningham[2], Sophia Schumaecker[2], Skylar Davis[2], Francesca Azar[3], Tzu-Yu Alkaid Feng[3], Maosen Wang[2], Melanie Rutkowski[3] & Jennifer Munson[1,2]

Systemic chemotherapy often affects cells beyond the tumor, raising concerns about their impact on peripheral tissues, including the central nervous system (CNS). The meningeal lymphatics drain cerebrospinal fluid from the CNS to the deep cervical lymph nodes, assisting in immunosurveillance and linking the CNS to the periphery. They have been implicated in a number of brain-related disorders with disruption exacerbating cognitive deficits. However, in vivo, distinguishing between direct and indirect effects of systemic chemotherapy on the meningeal lymphatics remains highly challenging, making it difficult to isolate specific impact on the CNS. To address this, we present two models we have developed that allow the examination of cellular and tissue-level changes to study the effects of systemic chemotherapy on the meningeal lymphatics. Our in vitro tissue engineered model representative of a meningeal lymphatic vessel lumen shows cell disruption, while our ex vivo model culturing mouse meningeal layers probes structural changes in a controlled setting. Finally, we correlate functional outcomes with observed changes in vivo and show that systemic taxane chemotherapy leads to morphological changes in the meningeal lymphatics, a trend of reduced flow through the brain, and impaired cognition, emphasizing the need for further study of off-target impacts in the CNS and the value of multi-model approaches.

The meningeal lymphatics (MLs), responsible for draining the central nervous system (CNS)[1,2], reside within the dura mater, the tough outermost layer of the meninges. Together with other layers within the meninges, the dura mater provides insulation between the skull and the brain[3]. Most notably, the meninges also serve as an immune cell reservoir and facilitate drainage of cerebrospinal fluid (CSF) and interstitial fluid from the CNS[4,5] to the cervical lymph nodes[2,6]. These processes are largely mediated by a specialized lymphatic network comprised of dural and basal meningeal lymphatic vessels. Previous studies have shown that the meningeal lymphatics are involved in brain tumor drainage[7,8], Alzheimer's disease[9,10], Parkinson's disease[11], and traumatic brain injury[12], with conservation between humans and mice[13]. Furthermore, in the context of treatments, they are critical in regulating anti-tumor immune response following radiotherapy[14]. Additionally, vascular endothelial growth factor receptor (VEGFR) inhibition through sunitinib treatment leads to regression in meningeal lymphatic vessels[15]. Though there are implications in cancer and cancer-related sequelae, the degree to which the meningeal lymphatics contribute to CNS pathophysiology in response to chemotherapeutic treatment has yet to be determined.

Chemotherapy is one of the most conventional forms of cancer treatment as a primary or adjuvant therapy alongside resection and/or radiotherapy. It has increased survival rates since its inception for a number of cancers. However, there are still known and unknown risks and side effects[16,17]. One significant reported effect is reduced cognitive performance in patients who receive chemotherapy, often referred to as "chemobrain" or "brain fog". Changes to the CNS indicate that these side effects could be due to inflammation, reduced neurogenesis, altered neuronal synapses and myelination, to name a few, though other causes may still exist[18]. Most chemotherapeutics are intravenously delivered to patients, circulating throughout the body to enter the tumor through the blood vasculature, while also coming into contact with all tissues. After entering the blood vasculature, chemotherapy drains through the tissue and towards the

---

[1]Department of Biomedical Engineering and Mechanics, Virginia Tech, Blacksburg, VA, 24061, USA. [2]Fralin Biomedical Research Institute, Roanoke, VA, 24016, USA. [3]Department of Microbiology, Immunology, and Cancer Biology, School of Medicine, University of Virginia, Charlottesville, VA, 22903, USA. [4]These authors contributed equally: L. Monet Roberts, Jennifer H. Hammel. ✉e-mail: monetr@vt.edu; munsonj@vt.edu

lymphatics, where it can have counter-therapeutic effects. Systemic chemotherapy recapitulating a standard-of-care breast cancer treatment regimen using either carboplatin or docetaxel in pre-clinical models leads to lymphangiogenesis in the primary tumor site and draining lymph nodes that can promote invasion of tumor cells[16,17]. However, the potential impact of chemotherapy on the distant meningeal lymphatics following systemic circulation in breast cancer is not defined. One reason is that dissecting out distinctive effects on near versus distal tissues can be a challenge in preclinical cancer models.

With renewed interest in the meningeal lymphatics, the development of both in vitro and ex vivo models is essential for addressing key biological questions and understanding the physiology of this critical lymphatic system. Further, isolating the meningeal compartment from the overall CNS may reveal tissue-specific effects on the meningeal lymphatics without confounding brain interactions. In vitro models allow the examination of crosstalk between cell types in an isolated and customizable system[19,20], while ex vivo systems preserve native tissue architecture, allowing for more physiologically relevant insights. Here, we developed an in vitro human cell–based model of the meningeal lymphatics alongside an ex vivo culture of mouse meningeal layers, leveraging these models to compare with in vivo studies and comprehensively assess the impact of chemotherapy on the meningeal lymphatics. Then, drawing from previous findings establishing that compromised meningeal lymphatics significantly contribute to cognitive dysfunction in mice[10], we determined the functional outcomes of docetaxel treatment on cognitive dysfunction and transport of fluid through the brain. Overall, our findings via multiscale models, paired with interrogating behavioral function in the presence of chemotherapeutics, indicate a role for the meningeal lymphatics in chemotherapy-related cognitive impairment while providing new models in which to study it.

Results

Development of an in vitro meningeal lymphatics model (ML model)

We developed an in vitro model of the meningeal lymphatics to probe chemotherapy response in a controllable, high-throughput setting. To represent the lumen of a meningeal lymphatic vessel, human lymphatic endothelial cells (LECs) were seeded and allowed to grow a complete monolayer on the underside of a tissue culture insert followed by human meningeal cells (MCs) seeded inside of the insert (Fig. 1A). To support optimal LEC viability, Vasculife® was selected as the culture media for the model (Supplemental Fig. S1). In Vasculife®, MCs had significantly more live cells per field of view compared to their preferred media, MenCM (Fig. 1B). Additionally, MC viability was unchanged between MenCM and Vasculife® (Fig. 1C). Barrier function of the model compared to monoculture controls was examined via dextran permeability assay where LECs had the lowest trend in barrier function compared to MCs alone and the ML model (Fig. 1D). Distinct monolayers were visualized in the complete model via CD31 and F-actin staining, overall demonstrating minimal transmigration and confirming integrity of our in vitro model (Fig. 1E).

LEC-MC crosstalk alters morphological response to platinum and taxane chemotherapy treatment

Informed by our previous studies examining the impact of standard-of-care platinum[17] or taxane[16] chemotherapy on dermal LECs alone, we used our in vitro model to examine the response to carboplatin and docetaxel treatment on the meningeal lymphatics using lymph node-derived LECs. Both the MCs and the LECs generated a complete monolayer when together in the ML model (Fig. 2A). Docetaxel treatment caused morphological changes in the MCs as they formed clumps or plaques (Fig. 2A and Supplementary Fig. S2A) in comparison with their standard fibroblastic morphology. In the ML model with LECs, MCs formed a significantly more complete monolayer, which was also sustained during chemotherapy treatment, compared to when cultured alone (Fig. 2B).

Carboplatin did not significantly decrease MC coverage in the ML model compared to the vehicle (Fig. 2B). MCs also had higher coverage in the ML model than alone when treated with docetaxel (Fig. 2B). Further, docetaxel caused significant disruption of the monolayer compared to the vehicle and carboplatin for both ML model and MCs alone (Fig. 2B). Additionally, MC count was not significantly different when alone compared to in the ML model after treatment with vehicle or carboplatin, but trended higher in the ML model for docetaxel-treated groups (Supplementary S2B). Since the overall cell count remained unchanged while the coverage area decreased for MCs, this suggests that the number of cells did not decline, but rather their ability to spread was possibly affected. Overall, MC coverage showed decreased disruption in the presence of LECs during chemotherapy treatment in the ML model.

LECs showed less benefit from culture in the ML model during chemotherapy treatment. Representative images indicated similarly intact monolayers of LECs (Fig. 2A and Supplementary Fig. S2A) in the vehicle and carboplatin-treated groups. However, docetaxel-treated groups had incomplete LEC monolayers and altered CD31 staining (Fig. 2A and Supplementary Fig. S2A). In the vehicle group, LEC coverage was unchanged between culture in the ML model and when cultured alone (Fig. 2C), but coverage disruptions by carboplatin treatment were reduced in the ML model (Fig. 2C). Additionally, LEC count (Supplementary Fig. S2C) was not significantly different between culture conditions for any of the chemotherapy groups. Notably, docetaxel significantly decreased LEC coverage in both the ML model and LECs alone (Fig. 2C).

In addition to coverage, LEC junctions, area, and aspect ratio were examined. LECs generally displayed more disrupted junctions when cultured alone than in the ML model (Supplementary Fig. S3A, B). Application of chemotherapy did not significantly increase junction disruption in LEC monocultures (Supplementary Fig. S3A, B). Yet, in the ML model, LECs displayed more disrupted junctions with docetaxel treatment (Supplementary Fig. S3A, B). LECs did not have significant changes to area across any groups or treatments (Supplementary Fig. S3C). However, LECs had a higher aspect ratio, meaning they were more elongated, when cultured alone compared to within the ML model in both the vehicle and carboplatin-treated groups (Supplementary Fig. S3D). Docetaxel treatment also resulted in increased elongation compared to all groups within the ML model (Supplementary Fig. S3D). These findings further suggest differences in cell spread and size that were dependent on both model incorporation and chemotherapy application.

LEC and MC proliferation are altered by chemotherapy in vitro

The mechanism of action of carboplatin and docetaxel relies on and can affect the proliferation of tumor cells, but it is known to affect non-tumor cells as well. Thus, we sought to identify whether crosstalk and chemotherapy altered the proliferation of MCs and LECs. At baseline, MCs had higher proliferation alone compared to within the ML model (Fig. 2D, E and Supplemental Fig. S4). Carboplatin did not change the proliferation of MCs in the ML model compared to MCs alone (Fig. 2D, E and Supplemental Fig. S4). Docetaxel-treated groups had very low levels of proliferation in both culture conditions and were significantly lower than all other groups (Fig. 2D, E and Supplemental Fig. S4).

Incorporation of LECs into the ML model did not significantly change their proliferation under any treatment conditions (Fig. 2D, F and Supplemental Fig. S4). Generally, LECs treated with docetaxel trended towards lower proliferation, but interestingly, while proliferation in the LEC-only control was not significantly reduced by docetaxel (Fig. 2F and Supplemental Fig. S4), LECs within the ML model displayed significantly lower proliferating cells with docetaxel treatment compared to carboplatin (Fig. 2F).

An ex vivo model of the meningeal lymphatics reveals chemotherapy-induced vasculature changes

Given the significant changes observed in our in vitro ML model, we wanted to determine whether these effects were conserved at a tissue level under direct chemotherapeutic treatment conditions. While in vitro models offer valuable insights into single-cell responses and high-throughput

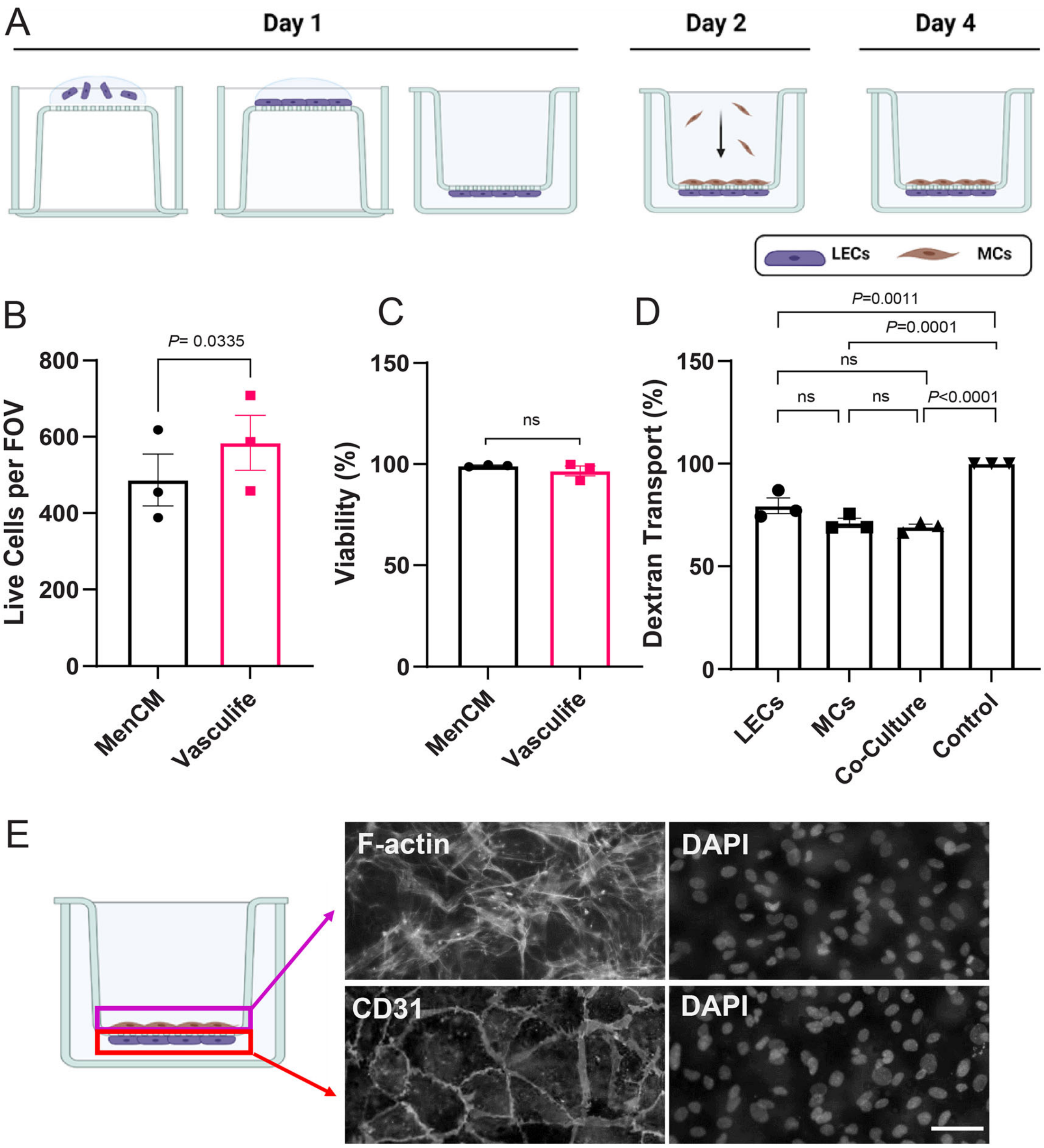

Fig. 1 | In vitro meningeal lymphatic model development. A Schematic representing the meningeal lymphatic model, where lymphatic endothelial cells (LECs) were seeded on the underside of a tissue culture insert for 2 h before inversion and culture for 24 h. Then, meningeal cells (MCs) were added to the tissue culture insert and cultured for an additional 36 h. **B** Quantitative analysis of media conditions for the ML model with MCs quantified both per field of view (FOV) and **C** percentage of viability in MenCM or Vasculife media. **D** Quantitative analysis of permeability of cells within the tissue culture model via dextran transport assay. **E** Representative images of each monolayer with MCs stained for F-actin (magenta box), LECs stained for CD31 (red box), and nuclei stained with DAPI. Data in bar graphs and error bars in (**B**–**D**) represent mean ± SEM ($n = 3$) with significance (**D**) determined via a one-way ANOVA ($p < 0.0001$) with a post hoc Tukey's multiple comparison test to calculate p-values. Scale bar is 50 µm.

functionality, our specific ML model lacks the morphological complexity seen in vivo. Therefore, we employed ex vivo meningeal layer tissue from Prox1-Tdtomato reporter mice to bridge the gap between observing treatment-induced effects and capturing the complex morphological architecture typically seen in vivo, while still enabling precise experimental manipulation. To confirm chemotherapeutic uptake within the tissue, we cultured ex vivo meningeal layers in the presence of 1 µM FITC-Docetaxel or vehicle (DMSO), where a clear fluorescent signal was observed within 3 h, indicating successful uptake (Supplementary Fig. S5).

After confirming uptake into the tissue, our ex vivo model provided a practical balance between physiological relevance and experimental control, enabling treatment application and visualization of features (Supplementary Fig. S5). However, during live imaging, the ability to consistently visualize changes in the meningeal tissue vasculature was challenging. Thus, we sought to observe lymphatic vasculature features and specific cellular responses at experimental endpoints.

In vivo, others have reported changes to the meningeal lymphatics that can be indicative of functional and biological changes, including the numbers of branching points[21] and intussusceptions/loops[10,22–25]. Thus, we examined these parameters in the context of chemotherapeutic treatment in our ex vivo model. Ex vivo meningeal layers were cultured and treated with either 1 µM of carboplatin, docetaxel, or vehicle (Fig. 3A), allowing us to assess both cellular- and tissue-level alterations within the native meningeal environment in a controlled manner similar to our in vitro approach. Intussusceptions/loops were markedly reduced in docetaxel-treated meningeal layers compared to vehicle treatment and were significantly

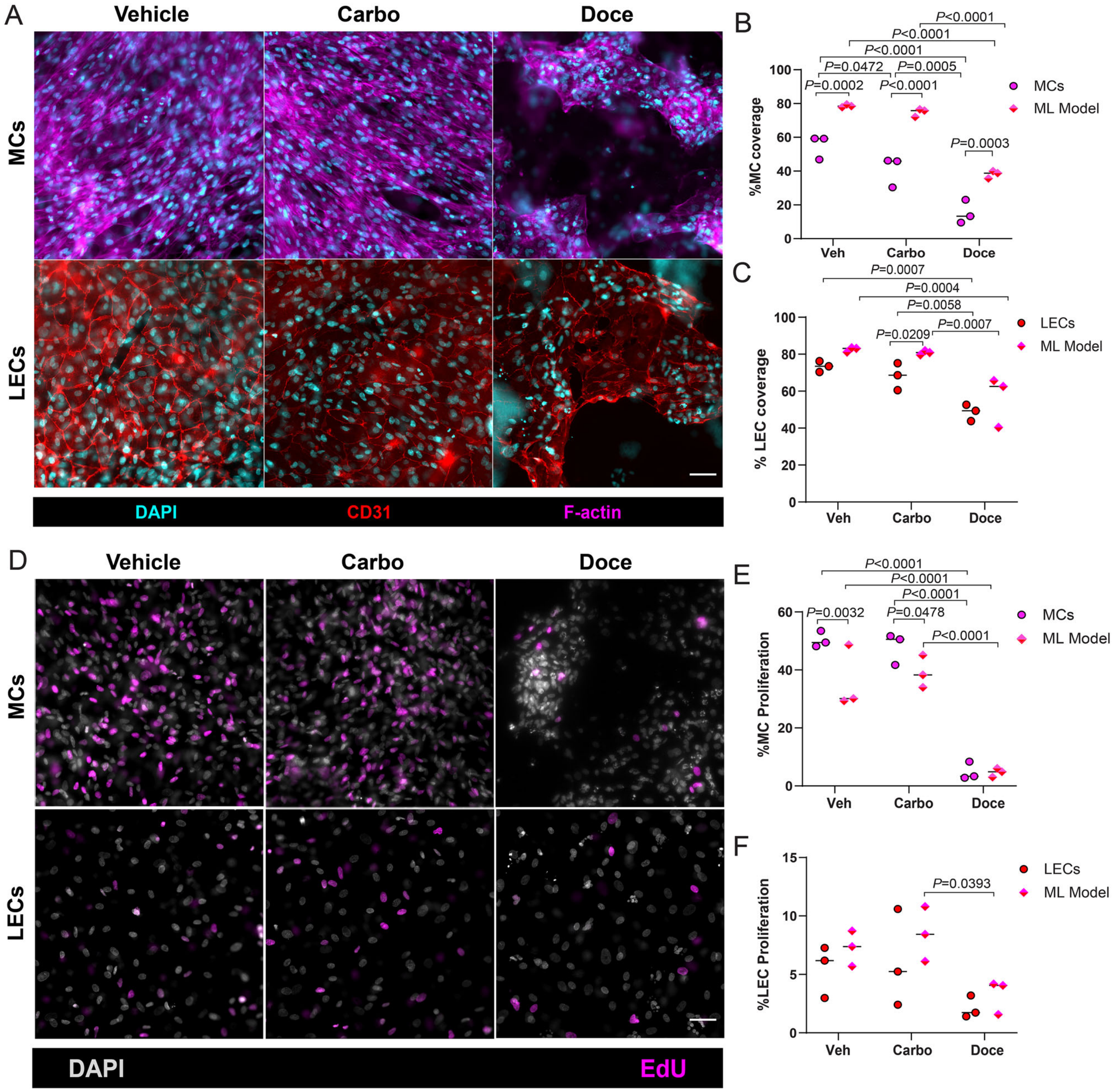

Fig. 2 | Docetaxel disrupts LEC and MC coverage and alters proliferation in vitro. ML models were treated with 1 μM carboplatin, 1 μM docetaxel, or vehicle (DMSO) for 24 h. **A** Representative images of ML models are shown with nuclei stained with DAPI (cyan), MCs stained for F-actin (magenta) and LECs stained for CD31 (red). Scale bar is 50 μm. Coverage of **B** MCs and **C** LECs was quantified via ImageJ and reported as a percentage within the ML model and as monocultures. For proliferation, 10 μM EdU was added to the culture media during the last 6 h of treatment. **D** Representative images of proliferation in the ML models are shown with all nuclei stained with DAPI (gray) and EdU-positive cells (magenta). Scale bar is 50 μm. The percentage of proliferation of **E** MCs and **F** LECs was quantified in ImageJ within the ML model and as monocultures. Data shown in B-F represent the mean and biological replicates of the data ($n = 3$) with significance determined via two-way ANOVA ($p < 0.01$ for each) between the vehicle and chemotherapeutic treatments with post hoc Tukey's multiple comparison test to calculate p-values (p-values of significance are solely represented). The data represent three experimental groups with reported p-values from comparisons, including a fourth experimental group, which is detailed in the supplementary material.

decreased compared to carboplatin treatment (Fig. 3B, C). Correlatively, the number of branching points was also lower, yet not significant, following treatment with docetaxel compared to both vehicle and carboplatin treatment (Fig. 3B, D).

Based on the changes in vasculature features that we observed in the tissue and effects of cellular proliferation in our in vitro ML model in response to docetaxel, we were then interested in linking structural changes to the proliferation of cells within the ex vivo meningeal tissue. Ex vivo meningeal layers were first treated with 1 μM FITC-Docetaxel or vehicle, along with EdU treatment for 6 h, as previously performed in our ML model. Following this initial incubation, the media was replaced with fresh treatment media and tissues were maintained for a total of 18 h of incubation with chemotherapeutics. Fluorescent detection of EdU incorporation for assessing cellular proliferation and additional immunostaining to evaluate vasculature remodeling were performed at the experimental endpoint. Interestingly, representative images revealed a higher number of EdU-positive cells in close proximity to identifiable meningeal lymphatic vessels, as indicated by LYVE-1 co-localized with Prox1, compared to regions of the

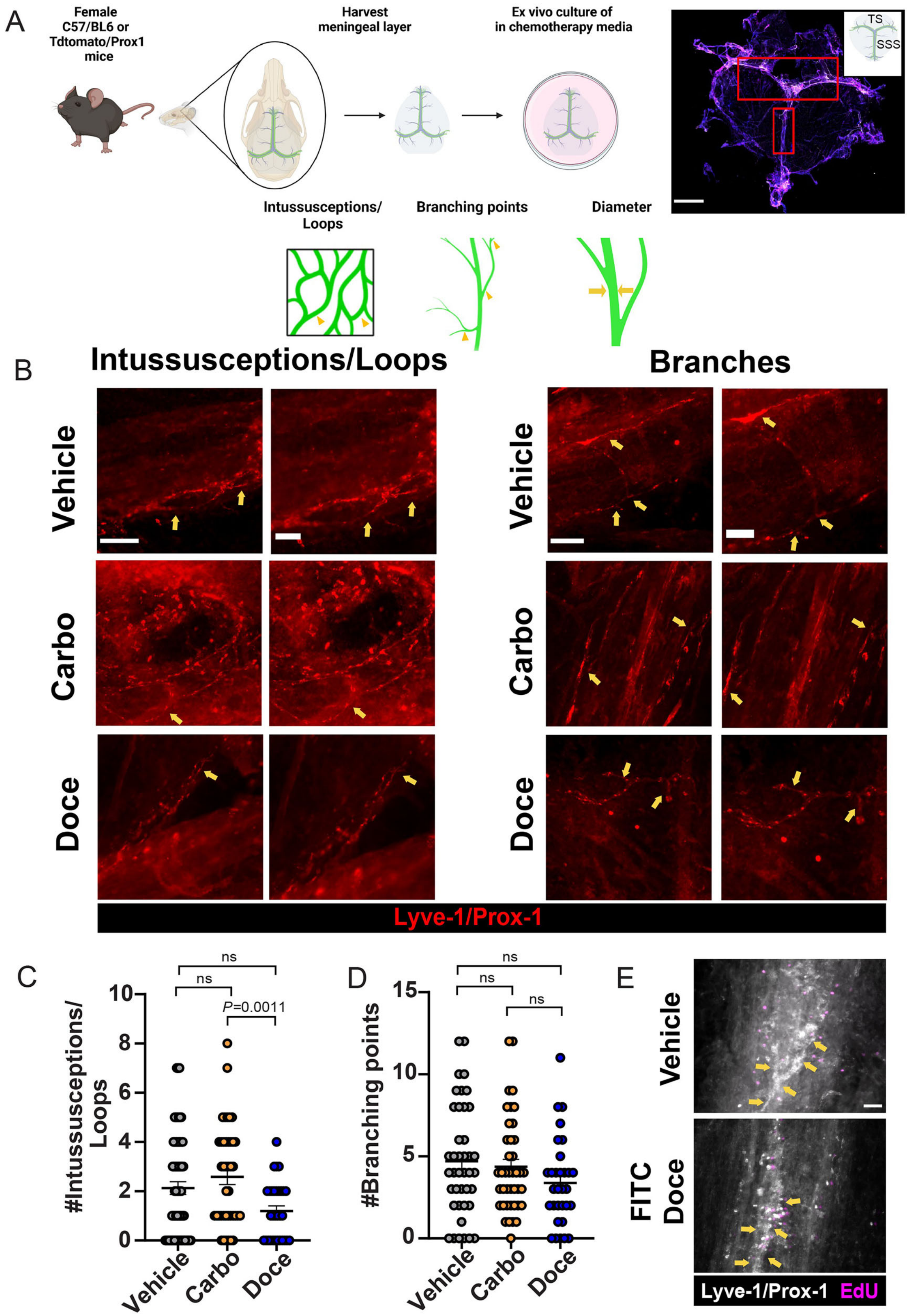

tissue that did not show considerable LYVE1/Prox1 signal, which we considered as "away" from these lymphatic vessels (Fig. 3E and Supplementary Fig. S6A, B). These findings suggested spatial differences in cellular proliferation regardless of treatment conditions. Most notably, proliferation was significantly different between specific dural lymphatic initiating vessels that drain interstitial fluid[2] known as the transverse sinus (TS) and the superior sagittal sinus (SSS), in the presence of FITC-Docetaxel. Significantly greater EdU-positive cells were observed in the TS in the presence of FITC-Docetaxel relative to the SSS (Supplementary Fig. S6C, D), though overall proliferation was not significantly different compared to vehicle treatment in either the TS or the SSS (Supplementary Fig. S6D, E). However, intussusceptions/loops and branching trended lower in both sinuses, yet no

Fig. 3 | Docetaxel decreases lymphatic remodeling and induces spatial proliferation in ex vivo murine meningeal layers. A (left) Workflow schematic of ex vivo culture of meningeal layers. (right) Representative image of a meningeal layer highlighting the superior sagittal sinus (SSS) and transverse sinus (TS) (red boxes; inset: cartoon represents the meningeal layer with the SSS and the TS denoted) (scale bar: 2 mm). (lower, middle) Schematic representing meningeal lymphatic vessel remodeling outcomes for analysis: intussusceptions/loops, branching, and diameter (features denoted by yellow arrows). **B** Representative images of intussusceptions/loops (left) and branches (right) in ex vivo meningeal layers in the presence of 1 μM carboplatin, 1 μM docetaxel, or vehicle for 24 h (features denoted by yellow arrows). Scale bar is 100 μm (left) and 50 μm (right, zoom). Quantification of **C** intussusceptions/loops and **D** branching points in ex vivo meningeal layers in the presence of carboplatin, docetaxel, or vehicle ($n = 4$). **E** Representative images of EdU-positive cells in ex vivo meningeal layers in the presence of 1 μM vehicle or FITC-Docetaxel ($n = 3$) (vessels denoted by yellow arrows). Scale bar is 50 μm. All graphs and error bars represent mean ± SEM. Significance was determined by one-way ANOVA ($p = 0.0183$) with post hoc Tukey's multiple comparison test to calculate represented p-values. The data represent three experimental groups with reported p-values from comparisons, including a fourth experimental group, which is detailed in the supplementary material.

differences were significant (Supplementary Fig. S6D, F). Overall, direct treatment with FITC-Docetaxel of ex vivo meningeal lymphatic layers resulted in regression of vessel features. Importantly, our ex vivo model preserves key structural characteristics of the native meningeal lymphatic vasculature, enabling the controlled study of chemotherapeutic effects on both cellular and vascular architecture in a physiologically relevant context.

Systemic chemotherapy induces morphological changes in lymphatic vasculature in 4T1 tumor-bearing mice

Cognitive deficits have been highly reported in breast tumor patients following chemotherapy with symptoms including loss of memory, learning, focus, and attention, which can persist even months or years after treatment[26–31]. Prior studies in other neurological conditions have linked meningeal lymphatic compromise to the conferral of learning behavior deficits in mice[10]. Thus, we sought to examine changes to the meningeal lymphatics in 4T1 tumor-bearing mice treated with systemic 8 mg/kg carboplatin or docetaxel based on prior published treatment regimens[16,17] (Fig. 4A). The dural meningeal layers were harvested one week after treatment concluded and analyzed for lymphatic vessel diameter, number of intussusceptions/loops, and number of branching points along the SSS and TS (Fig. 4B, C, Supplementary Video S1, Supplementary Fig. S7). The average diameter of the lymphatic vessels in response to docetaxel trended lower than both carboplatin and vehicle treatment (Fig. 4B-D and Supplementary Fig. S8A–C). However, docetaxel treatment resulted in significantly decreased numbers of intussusceptions/loops compared to vehicle- and carboplatin-treated mice with a trend towards lower branching points (Fig. 4B, C, E, F). Based on the interesting trends seen ex vivo, we sought to explore differences in lymphatic structure between the SSS and the TS. Though there was no difference in the diameter of vessels or branching within the SSS and the TS (Supplementary Fig. S8B), we did observe a significant decrease in intussusceptions/loops in docetaxel-treated mice as compared to carboplatin and vehicle in the TS (Supplementary Fig. S8C).

Combination treatment of carboplatin and docetaxel does not significantly differ from docetaxel-only conditions in vitro, in vivo, and ex vivo

Since many patients receive combinations of chemotherapies, we also performed a subset of studies wherein we examined treatment with both carboplatin and docetaxel (Supplementary Fig. S9). In vitro, combination treatment was significantly more deleterious than carboplatin alone in terms of disrupted coverage of both cell types and decreased proliferation of MCs. However, combination therapy was not significantly different from docetaxel-only groups (Supplementary Fig. S9A–D). In vivo, combination treatment induced significantly fewer intussusceptions and loops than carboplatin alone but was not significantly different from docetaxel (Supplementary Fig. S9E). However, in our ex vivo model, we were not able to detect any substantial differences in structural feature changes with combination treatment (Supplementary Fig. S9F). Overall, these findings suggest that combination treatment with carboplatin does not alter effects observed with docetaxel alone across in vitro, in vivo, and ex vivo, further underscoring the potent and independently deleterious impact of docetaxel on meningeal lymphatic vasculature structure and function.

Docetaxel treatment in naïve mice indicates potential chemotherapy-induced functional and neurological effects on meningeal lymphatics

Given that we observed structural feature alterations in meningeal lymphatics both in 4T1 tumor-inoculated mice and naïve ex vivo meningeal layers in response to docetaxel, we aimed to further investigate whether these changes were accompanied by functional outcomes, particularly related to drainage. Compromised drainage is considered a significant contributor to learning behavior deficits in mice across a number of neurological disorders and conditions[10,12,32]. Since we observed the most striking changes with docetaxel treatment, we set out to determine if there were any associated memory and learning behavioral deficits. Thus, we treated tumor naïve mice systemically with either 8 mg/kg docetaxel or vehicle and tested behavioral memory changes using novel object recognition (NOR) and passive avoidance (PA) tests (Fig. 5A). No differences in PA latency were detected between the groups within the training period; however, docetaxel-treated mice had significantly decreased step-through latency compared to the vehicle group on the test day (Fig. 5B). NOR testing revealed that vehicle-treated mice displayed a significantly increased propensity to explore the novel object than the familiar one as compared to the docetaxel-treated mice which showed no preference between the novel nor familiar object (Fig. 5C, D, E). Thus, on these tests, docetaxel reduced the memory-related performance in mice.

Since we observed structural changes in meningeal lymphatics in our breast tumor mouse studies in response to docetaxel treatment, we confirmed that docetaxel similarly impacted meningeal lymphatic features without the confounding factor of tumor presence in naivemice. Intussusceptions/loops were significantly decreased as a result of docetaxel treatment compared to vehicle (Fig. 5F), with no significant difference in branching points similar to what we observed in our tumor in vivo studies (Figs. 5G and 4B–F). Overall, systemic docetaxel conferred regression of meningeal lymphatic vessel structure.

As the main conduit for drainage of waste from the brain and CNS, we then wanted to assess whether meningeal lymphatic structural changes observed in response to docetaxel treatment also correlated with altered fluid flow in the brain. Prior studies have connected meningeal lymphatic drainage to overall fluid flow and transport within the brain parenchyma[33]. Thus, we assessed transport in the brain through the application of T1-weighted dynamic contrast-enhanced magnetic resonance imaging (DCE-MRI) after injection of a gadolinium-based contrast agent. Coupling the imaging with our previously published analysis method, which uses the images to solve the mass transport equation, we generated maps of interstitial transport across the mouse brain. As seen in prior studies, magnitude maps demonstrate a range of flow velocities between 0.043-1.516 μm/s throughout the whole brain (Fig. 5H). When comparing groups, overall flow magnitude trended downward with docetaxel treatment (Fig. 5I). Since the hippocampus and prefrontal cortex are important in memory and learning, we also measured flow only in these regions (Supplementary Figs. S10, S11 and Fig. 5J, K). Overall, we saw similar trends of overall decreased flow magnitude with docetaxel treatment, independent of location. Overall, though there were no significant changes due to high variability within individual mice, there are potential trends towards decreasing flow in mice treated with docetaxel.

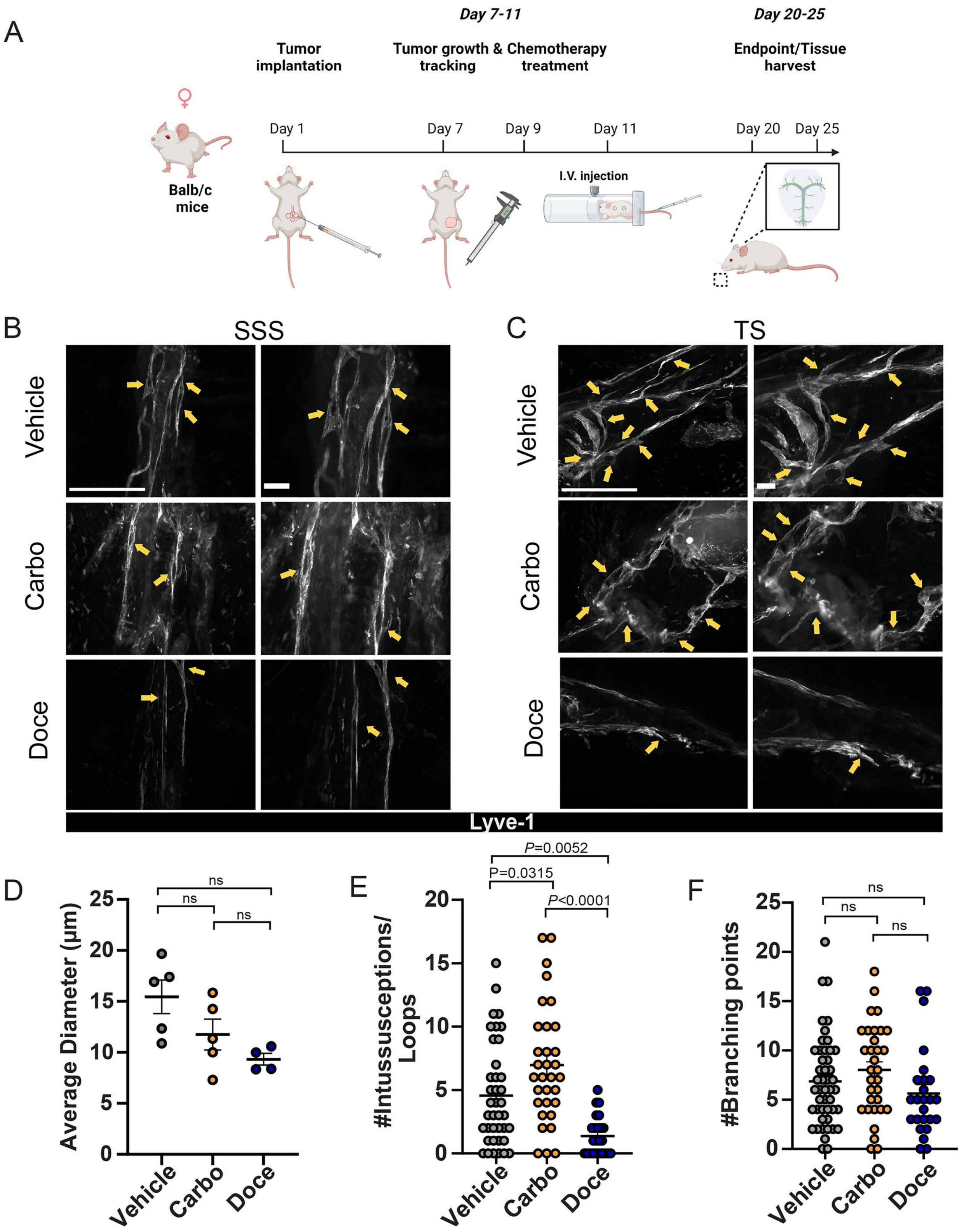

In order to leverage the design of the study wherein multiple outcomes were examined in a single mouse, multiple correlation analysis for vehicle and docetaxel-treated tumor naïve mice was conducted. In passive avoidance testing, there was a very weak correlation between the number of intussusception/loops in the meningeal lymphatic vessels and latency time in the dark chamber in PA testing ($r = 0.14$, $p > 0.05$) in vehicle-treated mice. Docetaxel treatment only resulted in a strong correlation between the number of intussusceptions/loops and the latency time that the mouse stayed in the dark chamber ($r = 0.89$, $p < 0.05$). Similarly, although not significant, the number of branching points followed a similar trend compared to latency time in PA testing ($r = 0.87$, $p = 0.055$ in

Fig. 4 | Meningeal lymphatic feature changes vary in response to different chemotherapeutic agents in tumor-bearing mice. A Schematic representation of the timeline and in vivo experimental layout where mice were inoculated with breast mammary tumor cells in the mammary fat pad and treated with chemotherapeutics via tail vein prior to harvesting of the dural meningeal lymphatic layer. **B** Representative images of intussusceptions/loops and **C** branching points in murine meningeal layers in response to systemic 8 mg/kg of vehicle, carboplatin, or docetaxel treatment (features denoted by yellow arrows). Scale bar is 500 µm (left) and 100 µm (right, zoom). **D** Quantification of the average diameter of meningeal lymphatic vessels in the presence of chemotherapies and vehicle. **E** Quantification of intussusceptions/loops and **F** branching in meningeal layers (Data is represented as an average from at least 20-30 points per experimental group). Significance was determined by a one-way ANOVA ($p < 0.0001$) with post hoc Tukey's multiple comparison test to calculate represented p-values. All graphs and error bars represent Mean ± SEM ($n = 5$ for vehicle and carboplatin, $n = 4$ for docetaxel). The data represent three experimental groups with reported p-values from comparison, including a fourth experimental group, which is detailed in the supplementary material.

docetaxel-treated; $r = 0.25$, $p > 0.05$ in vehicle-treated mice). No significant correlation was seen with MRI outcomes and performance on PA testing.

In NOR testing, there was a strong correlation between the number of intussusceptions/loops within the meningeal lymphatics and percentage of time with the familiar object in the NOR test in vehicle-treated mice, but not in the docetaxel-treated mice ($r = 0.87$, $p = 0.058$ compared to $r = 0.26$, $p = 0.678$ with docetaxel treatment). Surprisingly, there was little to no correlation in intussusceptions/loops and branching points compared to the magnitude in the hippocampus and cortex. Overall, it was interesting to see that some physiological changes correlated with key behavioral outcomes, and that docetaxel could change the strength of the correlation, indicating a connection among these experimental elements.

Discussion

We and others have shown that the meningeal lymphatics are involved in drainage and cognitive function in a number of neurological conditions[10,12,32]. Cognitive impairment is commonly reported by patients who have had chemotherapeutic treatment[34,35]. Specifically, cognitive dysfunction has been associated with docetaxel and other standard-of-care taxane therapeutics in both rodents[36–40] and humans[29,30]. However, the impact of platinum chemotherapy on cognitive function is less clear[41,42]. In an effort to link structural features and functional changes as a result of systemic docetaxel treatment, we conducted behavioral testing and DCE-MRI to assess any impact on memory/learning changes and brain region-specific drainage. From our results, we showed decreased novel object recognition memory function and increased latency in docetaxel-treated mice compared to saline treatment. The decreased meningeal lymphatic features, particularly intussusceptions/loops, observed in docetaxel-treated mice were also strongly correlated with some of the memory deficits in mice. These results emphasize that meningeal lymphatic vascular features have an impact on large-scale functional changes. Results from our MRI studies did not show a significant difference within the hippocampal regions of the brain critical to memory and learning, which we found surprising. However, we did see a downward trend in flow magnitude. It is possible that differences in flow rate from mouse to mouse are a confounding factor that requires higher replicate counts.

Of note, the ages of our mice ranged from 6 weeks to 12 weeks old, which is representative of fully developed adults. Age-induced structural feature changes of mice meningeal layers, fluid flow and drainage in the brain, and memory/learning outcomes have been previously shown in mice aged 20-24 months old[10]. Across the ranges of ages that our adult mice represented, we are confident that the changes we are seeing are due to docetaxel treatment solely. Future considerations of aging and its impact on meningeal lymphatic structural features and function in the context of chemotherapeutic treatment. Since aging is also a known risk factor in cognitive function and drainage, it is also a known prognostic factor for poorer outcomes in cancer. Therefore, it will be interesting to examine how aging influences treatment outcomes and overall brain health.

Though we saw a non-significant yet trending decrease in interstitial flow in the brain in response to systemic chemotherapy, more dramatic changes could be occurring in downstream lymph nodes or collecting vessels more easily accessed by chemotherapy. Thus, future studies to examine total outflow and drainage of fluid through meningeal lymphatics to the cervical lymph nodes will be needed to better represent the correlations of fluid flow, memory/learning, and the meningeal lymphatics. Overall, in parallel with our findings from our ex vivo and in vitro studies, results were not in the presence of a tumor, as most of the reported cognitive effects are documented, further solidifying that docetaxel treatment definitively causes these deleterious effects.

Through our previous studies, we have established that platinum and taxane systemic chemotherapy impacts lymphatics in mammary fat pads, ex vivo mesentery lymphatics, and lymphatic endothelial cells in vitro[16,17]. Building upon these previous findings, our in vitro ML model yielded interesting insights regarding cellular behavior and proliferation that correlate with the mechanisms of action of the chemotherapeutic agents used. Carboplatin, a platinum-based chemotherapy, prevents proliferation by binding to DNA, inhibiting replication, and triggering apoptosis[43]. Docetaxel, a taxane chemotherapy, interferes with microtubules, leading to cell cycle arrest and preventing cell division[44,45]. These chemotherapies are known to have off-target side effects as they can often impact rapidly dividing healthy cells, such as hair, nails, and skin. Our work, along with others, has shown that chemotherapeutics can disrupt the delicate balance between lymphatic structural maintenance and function. Docetaxel, in particular, has been shown to cause lymphatic dysfunction with lymphedema being a common side effect following breast cancer treatment[46–48]. Previous studies have also shown that docetaxel accumulates in the lymphatics following both subcutaneous and intravenous delivery, whereas carboplatin does not[49]. Following delivery, the drug is distributed through the bloodstream and, once it reaches the carotid canal, it feeds into a collection of arteries that pass through the CNS, primarily the middle meningeal artery[50]. Blood then circulates through the superior sagittal sinus in the dura[51], likely serving as a conduit in exposing the meningeal lymphatics to the drug. Additionally, systemic chemotherapies are known to accumulate in the CSF[52–54] with docetaxel being previously shown to accumulate in low doses with reduced clearance from the CSF compared to the blood[52]. Notably, while docetaxel cannot cross the blood-brain barrier (BBB), this further supports that it accumulates in the meninges through their unique blood supply. This may lead to exposure to higher concentrations in the meningeal lymphatics as it serves as the primary system to drain the meninges. Moreover, though it cannot cross the BBB in its normal form, docetaxel has been associated with increased incidence of breast cancer metastasis to the brain, suggesting its potential to disrupt the BBB[53] and cause other forms of dysregulation in the CNS. Together, these findings strongly suggest that docetaxel specifically has multiple routes to get to the meningeal lymphatics and likely poses deleterious impacts on meningeal lymphatics as demonstrated here.

As such, we showed that docetaxel significantly altered meningeal lymphatic features in vivo and ex vivo, including intussusceptions/loops and branching points. This could possibly provide insights into fates in remodeling, such as perpetual branching with periendothelial cell networks splitting into intussusceptions as seen in blood vasculature[21], and lymphangiogenesis associated with lymphatic development and malfunction[22–25]. In contrast, in breast stroma, docetaxel induced lymphatic remodeling when the tumor was present but had no impact

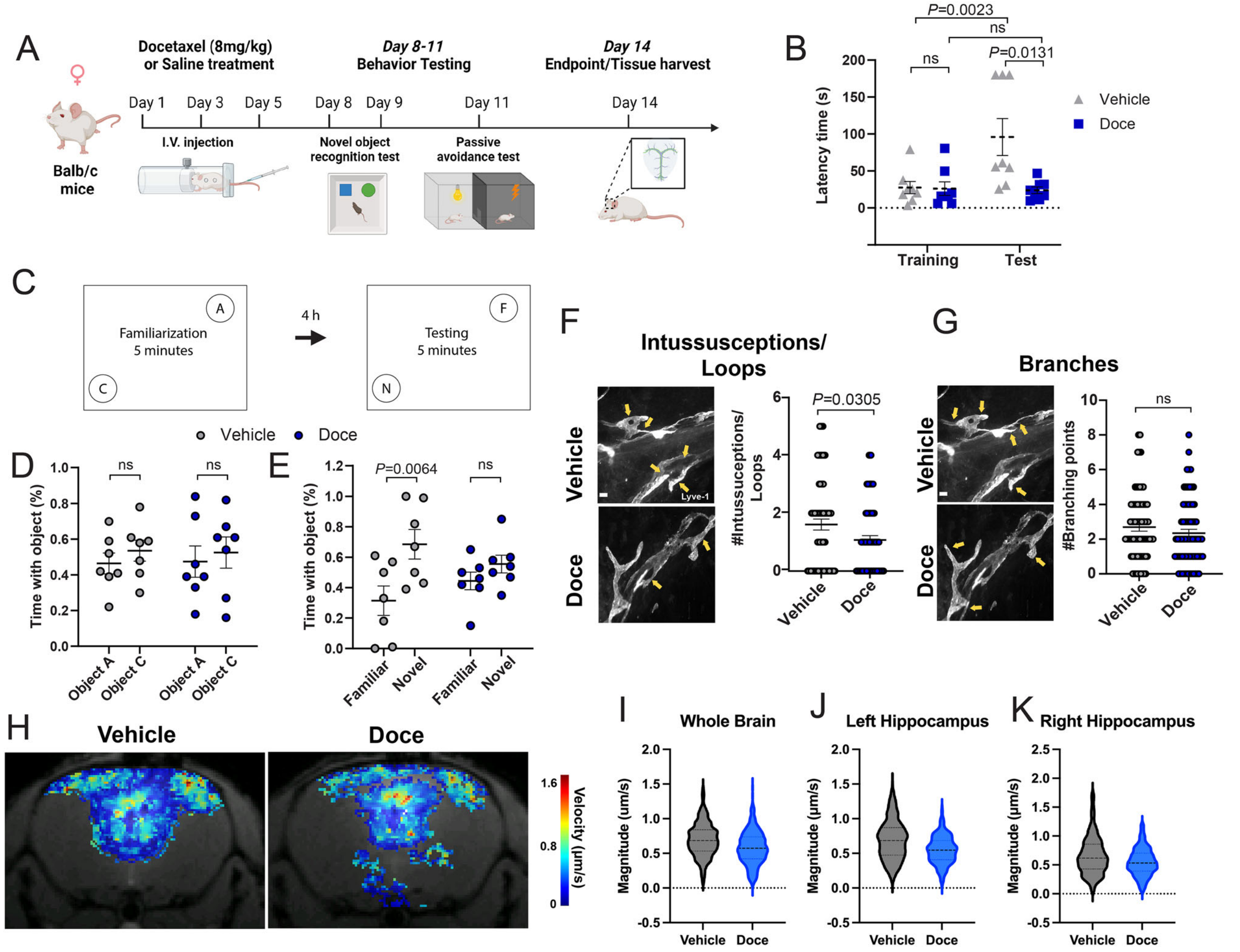

Fig. 5 | Docetaxel treatment confers a decline in memory, meningeal lymphatic feature changes, and lower whole brain and hippocampal fluid flow trends in tumor naïve mice. **A** Workflow schematic representation of the timeline and in vivo experimental layout where tumor naïve mice were treated with vehicle or docetaxel prior to NOR and PA testing, prior to harvest of the dural meningeal lymphatic layer. **B** Quantification of latency time in the dark platform in passive avoidance testing in response to treatment ($n = 8$). Significance was determined by a repeated measures two-way ANOVA ($p < 0.05$) with post hoc Holm-Šídák correction for multiple comparisons and represented p-values. **C** Schematic representation of details on familiarization and testing of object recognition. **D**, **E** Quantification of percentage of time with objects in the **D** familiarization phase and **E** introduction of the novel object in the NOR test in response to treatment ($n = 7$). Significance was determined by a repeated measures two-way ANOVA ($p = 0.006$) with a post hoc Bonferroni correction for multiple comparisons and represented p-values. **F** Representative images of intussusceptions/loops and **G** branching points in murine meningeal layers in response to 8 mg/kg of systemic vehicle or docetaxel (features denoted by yellow arrows). Scale bar is 50 μm. **H** Representative images of post-gadolinium T1-weighted images with overlaid velocity magnitude from interstitial fluid flow mapping in the whole brain of mice treated with either 8 mg/kg vehicle or docetaxel ($n = 3$). **I**–**K** Quantification of the magnitude of fluid flow in the **I** whole brain, **J** left hippocampus, and **K** right hippocampus in the brain of mice treated with 8 mg/kg of vehicle or docetaxel ($n = 3$ per treatment condition). Violin plots include every pixel value for each mouse. For statistical analysis, pixel values were averaged to give one value per mouse, followed by unpaired two-tailed Student's t-tests to determine statistical significance. All graphs and error bars represent the mean ± SEM, with the exception of box plots in **I**–**K**, which represent range and median.

without the tumor[16], thereby suggesting that the effects of docetaxel on lymphatic architecture may be context dependent.

Additionally, we saw location differences within the dural meningeal layer, detecting differences in proliferation and feature changes between the transverse sinus and superior sagittal sinus. Recent studies noted differences in structure and functionality at both locations, confirming the importance of spatial-based analysis in meningeal lymphatic studies[2,15,54,55]. In our studies, there were no significant differences between the average number of branches and intussusceptions/loops along the meningeal layer at the superior sagittal sinus as a result of docetaxel treatment compared to the vehicle. However, there was a significant decrease in intussusceptions/loops at the transverse sinus in meningeal layers in our in vivo studies. Waste and fluid flow containing chemotherapy drains through the meningeal lymphatics starting in the superior sagittal sinus prior to ultimately draining through the meningeal lymphatic vessels in the transverse sinus[56]. In assessing proliferation in our ex vivo studies, there were no significant differences in the number of features between the transverse and superior sagittal sinuses. However, we did note that there was increased proliferation at the transverse sinus. With drainage culminating at this site, our findings could possibly indicate enhanced regulation of cells at specific drainage locations.

In tandem with the established accumulation and impact of docetaxel in the lymphatics, other cells uptake chemotherapy, and certain highly proliferative cell types may be most affected. Within the dural meningeal layer, there are cell types with high turnover rates, most notably fibroblasts, which surround the meningeal lymphatic vessels[4,57]. Given the specific mechanism of action of docetaxel, we suspect that meningeal fibroblasts are particularly susceptible to its effects due to their proliferative nature. In

Table 1 | Comparison of attributes across the in vivo, ex vivo, and in vitro models for meningeal lymphatic analysis

	In vivo	Ex vivo	In vitro
Best for	Systemic treatment to mimic patient standard-of-care regimen, endpoint structural remodeling	Imaging of uptake, meningeal tissue and cellular features, endpoint structural changes and remodeling	Immune cell transmigration, cellular crosstalk, cell morphology, protein secretion
Scale	Bulk structure	Bulk structure	Cellular
Ease of study	Medium	Medium	High
Ability to test many conditions	Low	Medium	High
Model complexity	High	Medium	Low
Timepoints	Fixed timepoints	Dynamic and fixed	Fixed timepoints
Length of study	Weeks	Days	Days

support of this, we saw decreased proliferating MCs in vitro in docetaxel-treated groups. Moreover, remodeling of the lymphatics and fibroblasts paired with any associated cell death may induce inflammatory responses, resulting in the recruitment of immune cells. These inflammatory cells, such as macrophages, could lead to further damage within the meninges. Additionally, native immune cells, which reside within the meninges, would be particularly susceptible to chemotherapy and potentially killed with unknown consequences within the brain. Thus, in future iterations of the models and study, incorporation of immune cells such as macrophages or lymphocytes is of great interest toward studying these interactions. Additionally, changes to lymphatics and tissue morphology are both influenced by and can alter fluid flow[58,59]. Future applications of our models could be enhanced by perfusion through the layers or along lymphatic monolayers to better represent the natural lymphatic system. This would allow assessment of the impact of chemotherapeutics and fluid flow response on structural feature changes to simulate physiological conditions. Looking forward, the in vitro meningeal lymphatic model presented within can be tailored to a wide variety of applications, such as the examination of different pathologies with known meningeal effects.

There is potential for differences in LEC response based on source and physiological function. For instance, in this study, we used lymph node LECs, but other types, such as dermal LECs, were used in previous studies[17]. In this study, carboplatin did not change proliferation or cause disrupted junctions in contrast to docetaxel. In our previous work, although dermal LECs were activated by carboplatin and displayed disrupted junctions, docetaxel did not disrupt junctions[17]. Interestingly, dermal LECs have been previously shown to possess a decreased ability to migrate and form tubes when treated with docetaxel[60]. Overall, these findings demonstrate the importance of the LEC source and microenvironment in altering the response to chemotherapy. We also examined the impact of platinum chemotherapy on meningeal lymphatics since we previously reported that carboplatin induced increased lymphangiogenesis in lymphatics in healthy non-cancerous rat mesentery, mouse mammary fat pads, mouse lungs, and human omentum[17]. Contrasting our previous findings, carboplatin did not induce increased meningeal lymphangiogenesis compared to vehicle in vivo or ex vivo, nor caused disruption in our in vitro model. This highlights differences in the response to chemotherapy based on the location and primary function of the lymphatic system in question. Lymphatic vessels in different parts of the body experience various tissue microenvironments, chemokine signaling, and drainage conditions. The meningeal lymphatics specifically drain CSF, which has a different composition than the interstitial fluid that is drained by other lymphatic systems. Evidence shows that over half of the proteins found in CSF are unique to the CNS[61]. Thus, the response of the meningeal lymphatics to a therapeutic likely differs from other non-CNS draining lymphatics.

Although a plethora of tools and experimental methods can be applied to develop a better understanding of the meningeal lymphatics, most studies have been conducted in vivo, where the complexity of the CNS can obscure specific mechanisms. Here, we have employed a multiscale approach, integrating in vitro meningeal lymphatic models, ex vivo culture of meningeal layers, and in vivo treatments, to synthesize existing evidence and explore how standard-of-care chemotherapies impact meningeal lymphatic cellular behavior, tissue remodeling, and ultimately, memory and learning outcomes. There are no existing in vitro models that examine changes in both LECs and meningeal fibroblasts together to recapitulate meningeal lymphatic tissue composition. For this purpose, we developed a tissue culture insert model of the meningeal lymphatics that allows for examination of immune cell transmigration, cellular crosstalk, cell morphology, and protein secretion. To best replicate the dural meningeal environment while considering structural architecture and tissue integrity, we developed an ex vivo model that allows for controllable treatment and assessment of vessel architecture. Based on our findings in vitro and ex vivo showing changes in response to chemotherapy, we performed in vivo systemic chemotherapy treatments in mice with and without tumors. Here, we saw altered meningeal lymphatic morphology and functionality in line with some of our outcomes observed in vitro and ex vivo. Each experimental model we have presented provides different benefits, which we have summarized in Table 1. Overall, we find that each model offers a distinct methodology that can be tailored to a range of experimental questions. Our in vivo model offers high physiological relevance to mimic systemic treatment. Our ex vivo model offers a whole tissue structure without confounding variables from crosstalk with other tissues and organs. Finally, our in vitro model allows for the highest throughput and microenvironment control. Together, these models form a unique and practical platform for the study of meningeal lymphatic biology.

Conclusion

We have presented a three-tiered approach toward studying the meningeal lymphatics, which is an area of great interest in understanding CNS malignancy. In vivo studies allow for systemic treatment and tissue-level analysis. The ex vivo component allows for imaging of uptake and tissue-level structural insights, while providing a higher ease of experimentation in a controllable manner. Our in vitro meningeal lymphatic model allows examination on a cellular level, higher throughput, and customization based on application. Further, we have shown that the meningeal lymphatics have differing responses to platinum and taxane chemotherapy compared to other lymphatic systems in the body, thus demonstrating off-target effects on the CNS that require future studies. Finally, we have demonstrated that disruption of the meningeal lymphatics post-chemotherapy is directly correlated with cognitive dysfunction. This dysfunction, called "chemo-brain" is commonly experienced by patients undergoing systemic chemotherapy treatment. Further study is required to determine how to protect this vital drainage system to reduce these devastating side effects.

Methods

Cell lines

4T1 murine mammary carcinoma cells were purchased from the ATCC. Cell lines were authenticated using MAP testing and bi-monthly mycoplasma testing to ensure they were free of viral and other pathogens. To limit genetic drift, cells were maintained at low passage numbers and maintained as frozen stocks at −180 °C and expanded only for inoculation into mice. Tumor cell lines were cultured according to conditions outlined by ATCC. Human lymph node lymphatic endothelial cells (LECs) (Sciencell) were cultured on fibronectin-coated flasks in VascuLife® VEGF-Mv media (Lifeline Cell Technology). Human meningeal cells (MCs) (Sciencell) were cultured on poly-L-lysine-coated flasks in MenCM complete media (Sciencell).

Animals

All animal studies were approved by the Institutional Animal Care and Use Committee at Virginia Polytechnic Institute & State University and the University of Virginia. All animals were maintained in specific pathogen-free barrier conditions at the University of Virginia and Virginia Polytechnic Institute & State University. For tumor-inoculated studies, 6-week-old female Balb/c mice were purchased from Jackson Laboratories. Mice tumor implantation and chemotherapeutic treatments were performed as previously described[16,17]. Briefly, BALB/c mice were injected with 10^4 4T1 murine mammary carcinoma cells. Tumor cells were resuspended in a mixture of ice-cold phosphate-buffered saline (PBS) and 3.3 mg/mL Matrigel, in a total volume of 50 μL, into the fourth mammary fat pad. Tumor growth was monitored, and when tumors reached a volume of 10 mm total dimension, as measured using calipers, mice were monitored daily. If tumors reached no more than 15 mm total diameter, became ulcerated, or impaired the mouse's ability to ambulate, eat or drink, it was euthanized. Otherwise, all analyses were performed 20–25 days post-tumor injection. Beginning on day 7, carboplatin and docetaxel were administered intravenously using tail-vein injection at 8 mg/kg of body weight, with mice administered saline/20% ethanol as a control every other day over the course of 6 days. For tumor naïve magnetic resonance imaging (MRI) and behavior studies, 8–10-week-old female Balb/c mice were purchased from Jackson Laboratories. Chemotherapeutic treatments were performed as described in the tumor in vivo studies, followed by MRI within one week of the treatment endpoint. For ex vivo studies, 6-week-old female C57BL/6 and Prox1-Tdtomato mice were purchased from Jackson Laboratories.

Novel object recognition (NOR) test

The apparatus for NOR testing consisted of a black-walled square box measuring 40 × 40 × 40 cm. Mice underwent two days of habituation prior to testing. On the first day of habituation, mice were placed in the open-field box and allowed to move freely for 5 min. On the second day of habituation, two identical objects were placed diagonally opposite each other in the box, and the mice were allowed to explore freely for 5 min. Active exploration was defined as sniffing or approaching objects within 2 cm. Four hours later on the second day, one familiar object was replaced with a novel object, and the mice were allowed to explore freely for 5 min. The time spent on each object and the total distance traveled were assessed using a camera (Logitech) and video tracking software (ANY-maze). The percentage of time spent on each object or discrimination index was calculated as [(time with object A or C)/(time with object A + time with object C) × 100 (%)].

Passive avoidance (PA) test

The experimental apparatus (San Diego Instruments, San Diego, CA) consisted of two compartments: a light compartment and a dark compartment separated by a grid door. A stainless-steel shock grid floor was placed in the dark compartment. During the acquisition trial, mice were placed in the light compartment. After 30 s, the grid door between the compartments was opened. The step-through latency for the mice to enter the dark compartment was measured, and the door was closed. Immediately after the mice entered the dark compartment, an inescapable foot shock (0.25 mA for 3 s) was applied. The retention test was performed 4 h after the training trial in a similar manner without the electric shock, and the step-through latency to enter the dark compartment was recorded. The maximum cutoff time for step-through latency was 300 s.

Magnetic resonance imaging (MRI) and interstitial flow analysis

Catheter placement. 8-week-old female Balb/c mice were anesthetized and placed in a stereotaxic frame. A burr hole was drilled at the stereotactic coordinates (A/P: −0.3 mm, M/L: 0.9 mm, D/V: 2.5 mm) relative to the lambda for intraventricular injections into the third ventricle on one side of the brain. A cannula guide (8IC315GS4PKC, P1 Technologies, Roanoke, VA, USA) was implanted and secured with a dummy cap (8IC315DCS4SP, P1 Technologies, Roanoke, VA, USA) until small animal MRI scanning. Following anesthesia, the dummy cap was removed, and an internal cannula (8IC315IS4P01, P1 Technologies, Roanoke, VA, USA) was inserted into the cannula guide.

MRI imaging. Mice were imaged with a 9.4 T small animal MRI (Bruker BioSpec AVANCE NEO 94/20 USR, Ettlingen, Germany) equipped with 660 mT/m high power gradient and 20 mm RF surface coil. To confirm cannula placement, T2-weighted imaging was conducted using a rapid acquisition with relaxation enhancement (RARE) sequence with the following parameters: repetition time (TR) = 1800 ms, echo time (TE) = 40 ms, field of view (FOV) = 19.2 × 19.2 mm with a 192 × 192 matrix, slice thickness = 0.5 mm, number of slices = 16, with 9 averages. This was followed by T1 mapping to collect baseline intensity, followed by a 2D dynamic contrast-enhanced (DCE) T1-weighted fast low-angle shot (FLASH) sequence. One pre-contrast image was acquired before injecting gadolinium (0.2 mL/kg, BioPal) at a rate of 1 μL/min. To measure the interstitial fluid transport metrics, T1-weighted dynamic contrast-enhanced magnetic resonance imaging (DCE-MRI) was performed. First, a pre-contrast T1-weighted image was collected using a FLASH sequence using the following parameters: repetition time (TR) = 180 ms, echo time (TE) = 11 ms, field of view (FOV) = 19.2 × 19.2 mm with a 192 × 192 matrix, slice thickness = 0.5 mm, number of slices = 16, and 7 averages requiring a total acquisition time of 3 min and 20 s[62].

Post-processing and analysis. Pre- and post-injection images were registered to correct for animal movement across timepoints. Transport metrics were extracted from the DCE-MRI sequence using Lymph4D, a previously published and publicly available tool[63]. Lymph4D calculates optimal parameters of the two-dimensional diffusion-advection equation to determine the best-fit combination of velocity magnitude, advection direction, and diffusion coefficient that describes temporal changes in gadolinium concentration. Analysis was restricted to pixels within the brain parenchyma that contained observable gadolinium influx from the ventricular injection, identified based on the standard deviation of each pixel's time-signal intensity curve (σTSIC) over the imaging period. To ensure a focus on significant signal changes, only pixels with a σTSIC exceeding the background MRI noise σTSIC by more than one standard deviation were included. Fluid flow analysis was conducted across the whole brain and in two anatomical regions: left and right frontal cortices and hippocampi. The cortices and hippocampi were segmented, and the velocity magnitude and diffusion coefficient for all pixels that fell within this region and contained signal were included in the analysis.

Tissue processing, harvesting, imaging, and analysis of in vivo and ex vivo meningeal layers

For 4T1 tumor-inoculated and tumor naive in vivo studies, mice were euthanized via carbon dioxide asphyxiation and secondary euthanasia through intracardiac perfusion with PBS and subsequent intracardiac perfusion with 4% paraformaldehyde (PFA). Skull caps were collected and incubated for 18 h at 4 °C in 4% PFA. Following 18 h incubation, skull caps were transferred to fresh PBS and stored at 4 °C until harvest of meningeal layers. For ex vivo tissues harvested from tumor naive mice, dissected skull cap explants were transferred directly to explant media [DMEM + L-Glutamax (10567-014; Fisher Scientific)], 10% FetalPURE (Genesee Scientific), 2.5% penicillin-streptomycin and 2.5% 250 μg/mL amphotericin B[64] on ice until subsequent chemotherapeutic treatments of either vehicle (DMSO), 1 μM of carboplatin (Tocris Bioscience) or 1 μM docetaxel (Tocris Bioscience) alone or in combination in explant media and incubated at 37 °C for 24 h. Following chemotherapeutic treatment, skull caps were fixed for 18 h in 4% PFA at 4 °C. Following fixation, skull caps were rinsed with PBS and stored in fresh PBS at 4 °C. Harvesting of the dural whole-mount meningeal layers was achieved through dissection from skull caps. The meningeal layers were dissected from the occipital side of the skull cap, peeled from the skull, and stored in PBS at 4 °C until subsequent processing for immunostaining.

For live whole-mount ex vivo meningeal layer dissection and labeling for imaging, meningeal layers were harvested from tumor naive Prox1-Tdtomato fluorescent reporter mice without perfusion and gently dissected from skull caps using a Zeiss Axio Zoom microscope in sterile explant media with 5X Anti/Anti (ThermoFisher). The layers were transferred to a poly-L-lysine-coated 24-well glass-bottom dish with sterile Ringer's solution (102 mM NaCl, 5 mM KCl, 2 mM $CaCl_2$, 28 mM sodium lactate) with 1X Anti/Anti and flattened out as much as possible. 2 μM FITC-Docetaxel (Conju-Probe) or DMSO in sterile Ringer's/Anti/Anti solution was added to the well plate at equal volume to get a final concentration of 1 μM FITC-Docetaxel with Click-iT™ EdU 647 solution per protocol (ThermoFisher). Time-lapse images were acquired in 15 min intervals over 6 h before the remaining 12 h incubation, before fixation and further immunofluorescence staining and EdU detection as described below.

Tissue culture insert model

12-mm tissue culture inserts with 8 μm pore size (Corning) were inverted in 6-well plates. LECs were seeded on the underside of the insert at 50,000 per insert and cultured for 2 h before re-inverting in a tissue culture plate. After 48 h, 75,000 MCs were seeded within the tissue culture insert. The co-culture model was grown for an additional 24 h to reach confluence before assays were performed. At confluence, models were treated with 1 μM carboplatin, 1 μM docetaxel, or vehicle (DMSO) in Vasculife® for 24 h.

Permeability assays

300 μL of 10 μg/mL FITC dextran 10,000 MW, anionic, lysine fixable (Invitrogen) in basal Vasculife® was added inside the tissue culture insert. 300 μL of basal Vasculife® was placed underneath the insert. After 6 h, the media from underneath the insert was collected and analyzed on a CLARIOstar plate reader. Samples were compared to a control of 300 μL of 10 μg/mL FITC dextran diluted with 300 μL of basal Vasculife® to represent 100% transport.

Immunofluorescence

Tissue culture inserts were fixed in 4% PFA for 15 min. The membranes of each insert were carefully cut out and mounted on positively charged slides for staining. Donkey serum was used to block nonspecific binding. Membranes were stained with sheep anti-human CD31 (R&D) at a 1:40 dilution for 2 h at room temperature (RT), followed by donkey anti-sheep Alexa Fluor 647 secondary antibody (Invitrogen) at a 1:400 dilution for 1 h at RT. Membranes were then stained with 488 Phalloidin for F-actin (Invitrogen) at a 1:400 dilution and DAPI (Invitrogen) at a 1:5000 dilution for 45 min. Slides were then mounted with Fluoromount, allowed to dry overnight, sealed with nail polish, and stored at 4 °C. Slides were imaged on a Zeiss Axio Observer.

For meningeal whole mounts, tissues were stained in 24-well plates until mounting. Specifically, tissues were blocked in blocking buffer solution containing 0.5% triton-X 100, 2% bovine serum albumin, and 3% donkey serum in PBS for 1–2 h at RT. Tissues were then incubated in the following primary antibodies: rabbit anti-mouse LYVE-1 (Abcam) at a dilution of 1:100, rabbit anti-mouse Prox1 (Abcam) at a dilution of 1:200, mouse anti-mouse α-SMA (Abcam) at a dilution of 1:100, and goat anti-mouse CD31 (R&D Systems) at a dilution of 1:100 at 4 °C overnight. Tissues were rinsed 2X for 5 min each in permeabilization buffer and then incubated in donkey anti-mouse FITC (Fisher Scientific), donkey anti-rabbit Alexa Fluor 555 (Invitrogen), and donkey anti-goat Alexa Fluor 647 (Invitrogen) at dilutions of 1:200 for 1 h at RT. Tissues were then rinsed 2X in permeabilization solution and 2X in PBS. Tissues were incubated with DAPI for 5 min and then rinsed in PBS 2X for 10 min each and mounted on glass slides and allowed to dry completely. Images were acquired at 10X magnification using the Zeiss Axio Observer or Discover ECHO Revolution microscope. At least five regions of interest were imaged across the superior sagittal sinus and along the transverse sinus.

Proliferation assay

The Click-iT™ EdU Cell Proliferation Kit for Imaging, Alexa Fluor™ 488 dye (ThermoFisher) was utilized to quantify proliferation in the meningeal lymphatic (ML) model. During the last 6 h of culture, 10 μM EdU was added to the culture media. At 24 h, tissue culture inserts were fixed in 4% PFA. EdU was then detected as specified by the manufacturer. Finally, the insert membranes were stained for CD31 and αSMA as described above.

For EdU detection in the meningeal layer whole mounts, the Click-iT™ EdU Cell Proliferation Kit for Imaging, Alexa Fluor™ 647 dye (ThermoFisher) was used for 6 h of culture in sterile Ringer's solution/1X Anti/Anti solution, then removed and replaced with sterile Ringer's solution/1X Anti/Anti solution for the remaining 12 h and incubated at 37 °C. Following incubation for a total of 18 h, the meningeal layers were fixed with 4% PFA and underwent subsequent immunofluorescence staining with LYVE-1 and DAPI as described above. EdU was then detected as specified by the manufacturer.

Image quantification

For the total area of fluorescence in the tissue-engineered model, images were thresholded using Fiji and the total area of signal was measured. For proliferation, total nuclei were quantified via DAPI stain and proliferating cells were quantified via positive EdU staining. Proliferation was reported as a percentage of EdU-positive cells out of the total cell number. Analysis of lymphatic vessels was performed in the dural sinuses, specifically the superior sagittal sinus and transverse sinus, respectively. The number of branching points and intussusceptions/loops was counted at consistent regions of interest across the meningeal lymphatic vessels, with at least 20–30 individual values counted per layer as reported. Diameter measurements of the meningeal vessels were calculated through a CellProfiler pipeline[65] trained to identify vessels as objects. To determine vessel diameter, the 'meanRadius' measurement for each vessel object from the 'MeasureObjectSizeShape' module in CellProfiler was multiplied by two.

Statistics and reproducibility

All statistical analysis was conducted through Graphpad Prism 10.2.2 (GraphPad Software). One-way ANOVA was performed for groups of three or more with statistical significance indicated by $p < 0.05$. When significance was identified, post ad hoc *t*-tests (ratio paired or unpaired Student's *t*-test) were performed to assess significance between two groups, with $p < 0.05$ indicating significance. For three or more groups, corrections for multiple comparisons were performed via Tukey's multiple comparison test (statistical significance $p < 0.05$) unless otherwise indicated. For behavior outcomes through passive avoidance testing in response to treatment, a repeated measures two-way ANOVA (statistical significance $p < 0.05$) with Holm-Šídák correction for multiple comparisons was conducted. For behavior outcomes through NOR testing in response to treatment, a repeated measures two-way ANOVA (statistical significance $p < 0.05$) with Bonferroni correction for multiple comparisons was conducted. For statistical analysis of MRI data, the pixels were averaged to give one value per region per mouse, and unpaired two-tailed Student's *t*-tests were performed (statistical significance indicated by $p < 0.05$).

All graphs, unless otherwise specified, represent mean ± standard error with individual statistical results discussed with the presented data. For correlation between behavioral outcomes, tissue-level changes in the meningeal lymphatics, and fluid flow outcomes in tumor naïve studies, Pearson's correlation coefficients (r) were calculated and reported as discussed. All measurements were taken from distinct samples unless otherwise noted as repeated measures. Outliers were identified through the ROUT method via Graphpad to ensure that any data points deviating significantly from the overall distribution were properly addressed. If values were more than 2 standard deviations from the mean, then, where appropriate, values were excluded to ensure the robustness and accuracy of the results, and the final dataset was subjected to further analysis and reported without these outliers.

For in vivo studies, biological replicates were defined as individual mice, where animals were distributed randomly for treatment and vehicle groups. For in vitro studies, biological replicates were defined as independent experimental runs conducted on separate days to assess variability of each run across time. Technical replicates were defined as parallel samples within the same experiment used to assess the consistency and variability within the assay or technique, which were performed in triplicate for in vitro and ex vivo studies. The biological replicates for each experiment can be found in the corresponding figure caption. Raw data files are available via Figshare[66].

Reporting summary

Further information on research design is available in the Nature Portfolio Reporting Summary linked to this article.

Data availability

Data presented in the study are included in the article and supplementary material. Data and the CellProfiler pipeline are available upon request, and further inquiries can be directed to the corresponding authors. Numerical source data for the graphs can be found on Figshare: https://doi.org/10.6084/m9.figshare.c.7939814.v1.

Code availability

The Lymph4D code that was used for analysis of magnetic resonance images is available through GitHub: https://github.com/avaccari/Lymph4D.

Received: 19 December 2023; Accepted: 23 August 2025;

References

1. Aspelund, A. et al. A dural lymphatic vascular system that drains brain interstitial fluid and macromolecules. *J. Exp. Med.* **212**, 991–999 (2015).
2. Louveau, A. et al. Structural and functional features of central nervous system lymphatic vessels. *Nature* https://doi.org/10.1038/nature14432 (2015).
3. Ghannam, J. Y. & Al Kharazi, K. A. Neuroanatomy, cranial meninges. *StatPearls* https://www.ncbi.nlm.nih.gov/books/NBK539882/ (2023). (accessed 3 Apr 2025).
4. Derk, J., Jones, H. E., Como, C., Pawlikowski, B. & Siegenthaler, J. A. Living on the edge of the CNS: meninges cell diversity in health and disease. *Front. Cell Neurosci.* **15**, 703944 (2021).
5. Tavares, G. A. & Louveau, A. Meningeal lymphatics: an immune gateway for the central nervous system. *Cells* **10**, 3385 (2021).
6. Ahn, J. H. et al. Meningeal lymphatic vessels at the skull base drain cerebrospinal fluid. *Nature* **572**, 62–66 (2019).
7. Kanamori, M. & Kipnis, J. Meningeal lymphatics "drain" brain tumors. *Cell Res.* **30**, 191–192 (2020).
8. Hu, X. et al. Meningeal lymphatic vessels regulate brain tumor drainage and immunity. *Cell Res.* **30**, 229–243 (2020).
9. Jaffe, R. J., Dave, R. S. & Byrareddy, S. N. Meningeal lymphatics in aging and Alzheimer's disease. *Ann. Transl. Med.* **7**, S2–S2 (2019).
10. Da Mesquita, S. et al. Functional aspects of meningeal lymphatics in ageing and Alzheimer's disease. *Nature* **560**, 185–191 (2018).
11. Zou, W. et al. Blocking meningeal lymphatic drainage aggravates Parkinson's disease-like pathology in mice overexpressing mutated α-synuclein. *Transl. Neurodegener.* https://doi.org/10.1186/s40035-019-0147-y (2019).
12. Bolte, A. C. et al. Meningeal lymphatic dysfunction exacerbates traumatic brain injury pathogenesis. *Nat. Commun.* **11**, 4524 (2020).
13. Jacob, L. et al. Conserved meningeal lymphatic drainage circuits in mice and humans. *J. Exp. Med.* **219**, https://doi.org/10.1084/jem.20220035 (2022).
14. Zhou, C., Ma, L., Xu, H., Huo, Y. & Luo, J. Meningeal lymphatics regulate radiotherapy efficacy through modulating anti-tumor immunity. *Cell Res.* **32**, 543–554 (2022).
15. Antila, S. et al. Development and plasticity of meningeal lymphatic vessels. *J. Exp. Med.* **214**, 3645–3667 (2017).
16. Harris, A. R., Perez, M. J. & Munson, J. M. Docetaxel facilitates lymphatic-tumor crosstalk to promote lymphangiogenesis and cancer progression. *BMC Cancer* **18**, 718 (2018).
17. Harris, A. R. et al. Platinum chemotherapy induces lymphangiogenesis in cancerous and healthy tissues that can be prevented with adjuvant anti-VEGFR3 therapy. *Front. Oncol*. **12**. https://doi.org/10.3389/fonc.2022.801764 (2022).
18. Onzi, G. R. et al. Chemobrain in breast cancer: mechanisms, clinical manifestations, and potential interventions. *Drug Saf.* **45**, 601–621 (2022).
19. Hammel, J. H., Zatorski, J. M., Cook, S. R., Pompano, R. R. & Munson, J. M. Engineering in vitro immune-competent tissue models for testing and evaluation of therapeutics. *Adv. Drug Deliv. Rev.* **182**, 114111 (2022).
20. Hammel, J. H., Cook, S. R., Belanger, M. C., Munson, J. M. & Pompano, R. R. Modeling immunity in vitro: slices, chips, and engineered tissues. *Annu. Rev. Biomed. Eng.* **23**, 461–491 (2021).
21. Augustin, H. G. Tubes, branches, and pillars: the many ways of forming a new vasculature. *Circ. Res.* **89**, 645–647 (2001).
22. Díaz-Flores, L. et al. Intussusceptive lymphangiogenesis in vascular transformation of lymph node sinuses. *Acta Histochem* **121**, 392–399 (2019).
23. Díaz-Flores, L., Gutiérrez, R., Pino García, M., González-Gómez, M. & Carrasco, J. L. Intussusceptive lymphangiogenesis in the sinuses of developing human foetal lymph nodes. *Ann. Anat. Anatomischer Anz.* **226**, 73–83 (2019).
24. Díaz-Flores, L. et al. Intussusceptive angiogenesis and its counterpart intussusceptive lymphangiogenesis. *Histol. Histopathol.* **35**, 1083–1103 (2020).
25. Díaz-Flores, L. et al. Intussusceptive lymphangiogenesis in lymphatic malformations/lymphangiomas. *Anat. Rec.* **302**, 2003–2013 (2019).
26. Martín, B. R., Rodríguez, E. J. F., Galve, M. I. R. & Hernández, J. J. C. Study of chemotherapy-induced cognitive impairment in women with breast cancer. *Int. J. Environ. Res. Public Health* **17**, 1–13 (2020).
27. Quesnel, C., Savard, J. & Ivers, H. Cognitive impairments associated with breast cancer treatments: results from a longitudinal study. *Breast Cancer Res. Treat.* **116**, 113–123 (2009).
28. Wefel, J. S., Saleeba, A. K., Buzdar, A. U. & Meyers, C. A. Acute and late onset cognitive dysfunction associated with chemotherapy in women with breast cancer. *Cancer* **116**, 3348–3356 (2010).
29. Lange, M. et al. Decline in cognitive function in older adults with early-stage breast cancer after adjuvant treatment. *Oncologist* **21**, 1337–1348 (2016).
30. Zheng, F., Cao, P., Zhou, J., Li, C. & Norris, J. Study on neurologic and cognitive dysfunction in breast cancer patients undergoing chemotherapy with resting state fMRI. *World Neurosurg.* **149**, 388–396 (2021).
31. Whittaker, A. L., George, R. P. & O'Malley, L. Prevalence of cognitive impairment following chemotherapy treatment for breast cancer: a systematic review and meta-analysis. *Sci. Rep.* **12**, 1–22 (2022).
32. Wang, L. et al. Deep cervical lymph node ligation aggravates AD-like pathology of APP/PS1 mice. *Brain Pathol*. https://doi.org/10.1111/bpa.12656 (2019).

33. Ringstad, G. & Eide, P. K. Glymphatic-lymphatic coupling: assessment of the evidence from magnetic resonance imaging of humans. *Cell. Mol. Life Sci.* **81**, 1–14 (2024).
34. Winocur, G. et al. Neurobiological mechanisms of chemotherapy-induced cognitive impairment in a transgenic model of breast cancer. *Neuroscience* **369**, 51–65 (2018).
35. Henderson, F. M. E., Cross A. J. & Baraniak A. R. 'A new normal with chemobrain': Experiences of the impact of chemotherapy-related cognitive deficits in long-term breast cancer survivors. *Health Psychol. Open* **6**. https://doi.org/10.1177/2055102919832234 (2019).
36. Brown, T. et al. Cognitive impairment resulting from treatment with docetaxel, doxorubicin, and cyclophosphamide. *Brain Res*. **1760**, 147397 (2021).
37. Callaghan, C. K. & O'Mara, S. M. Long-term cognitive dysfunction in the rat following docetaxel treatment is ameliorated by the phosphodiesterase-4 inhibitor, rolipram. *Behav. Brain Res.* **290**, 84–89 (2015).
38. Fardell, J. E., Vardy, J. & Johnston, I. N. The short and long term effects of docetaxel chemotherapy on rodent object recognition and spatial reference memory. *Life Sci.* **93**, 596–604 (2013).
39. Liu, P. et al. Docetaxel-induced cognitive impairment in rats can be ameliorated by edaravone dexborneol: Evidence from the indicators of biological behavior and anisotropic fraction. *Front. Neurosci.* **17**, 1167425 (2023).
40. Li, Z. et al. Role of GABAB receptors and p38MAPK/NF-κB pathway in paclitaxel-induced apoptosis of hippocampal neurons. *Pharm. Biol.* **55**, 2188–2195 (2017).
41. Whitford, H. S. et al. The impact of chemotherapy on cognitive function: a multicentre prospective cohort study in testicular cancer. *Support. Care Cancer* **28**, 3081–3091 (2020).
42. Kaplan, S. V. et al. Impaired brain dopamine and serotonin release and uptake in wistar rats following treatment with carboplatin. *ACS Chem. Neurosci.* **7**, 689–699 (2016).
43. de Sousa, G. F., Wlodarczyk, S. R. & Monteiro, G. Carboplatin: molecular mechanisms of action associated with chemoresistance. *Braz. J. Pharm. Sci.* **50**, 693–701 (2014).
44. Herbst, R. S. & Khuri, F. R. Mode of action of docetaxel—a basis for combination with novel anticancer agents. *Cancer Treat. Rev.* **29**, 407–415 (2003).
45. Hernández-Vargas, H., Palacios, J. & Moreno-Bueno, G. Telling cells how to die: docetaxel therapy in cancer cell lines. *Cell Cycle* **6**, 780–783 (2007).
46. Akita, S. et al. Early detection of lymphatic disorder and treatment for lymphedema following breast cancer. *Plast. Reconstr. Surg.* **138**, 192e–202e (2016).
47. Park, S. I. et al. Clinical features of docetaxel chemotherapy-related lymphedema. *Lymphat. Res. Biol.* **12**, 197–202 (2014).
48. Béhar, A. et al. The pathophysiological mechanism of fluid retention in advanced cancer patients treated with docetaxel, but not receiving corticosteroid comedication. *Br. J. Clin. Pharm.* **43**, 653–658 (1997).
49. Worley, D. R., Hansen, R. J., Wittenburg, L. A., Chubb, L. S., & Gustafson, D. L. Docetaxel accumulates in lymphatic circulation following subcutaneous delivery compared to intravenous delivery in rats. *Anticancer Res.* **36**, 5071–5078 (2016).
50. Yu, J., Guo, Y., Xu, B. & Xu, K. Clinical importance of the middle meningeal artery: a review of the literature. *Int. J. Med Sci.* **13**, 790 (2016).
51. Bonasia, S., Smajda, S., Ciccio, G. & Robert, T. Middle meningeal artery: anatomy and variations. *Am. J. Neuroradiol.* **41**, 1777 (2020).
52. Ten Tije, A. J. et al. Limited cerebrospinal fluid penetration of docetaxel. *Anticancer Drugs* **15**, 715–718 (2004).
53. Bernatz, S. et al. Impact of docetaxel on blood-brain barrier function and formation of breast cancer brain metastases. *J. Exp. Clin. Cancer Res.* **38**, 1–21 (2019).
54. Hauglund, N. L., Kusk, P., Kornum, B. R. & Nedergaard, M. Meningeal lymphangiogenesis and enhanced glymphatic activity in mice with chronically implanted EEG electrodes. *J. Neurosci.* **40**, 2371–2380 (2020).
55. Jacob, L. et al. 3D-imaging reveals conserved cerebrospinal fluid drainage via meningeal lymphatic vasculature in mice and humans. https://doi.org/10.1101/2022.01.13.476230 (2022).
56. Letchuman, V. & Donohoe, C. Neuroanatomy, superior sagittal sinus. *StatPearls* (2023). https://www.ncbi.nlm.nih.gov/books/NBK546615/ (accessed 9 Aug 2023).
57. Wang, A. Z. et al. Single-cell profiling of human dura and meningioma reveals cellular meningeal landscape and insights into meningioma immune response. *Genome Med.* **14**, 1–25 (2022).
58. Rutkowski, J. M. & Swartz, M. A. A driving force for change: interstitial flow as a morphoregulator. *Trends Cell Biol.* **17**, 44–50 (2007).
59. Boardman, K. C. & Swartz, M. A. Interstitial flow as a guide for lymphangiogenesis. *Circ. Res.* **92**, 801–808 (2003).
60. Wong, A. M. et al. Docetaxel causes lymphatic endothelial cell apoptosis and impairs lymphatic function and gene expression in vitro. *J. Transl. Sci.* **7**, https://doi.org/10.15761/JTS.1000402 (2021)
61. Schutzer, S. E. et al. Establishing the proteome of normal human cerebrospinal fluid. *PLoS ONE* **5**, e10980 (2010).
62. Carman-Esparza, C. et al. A novel methodology for mapping interstitial fluid dynamics in murine brain tumors using DCE-MRI. *Methods* **231**, 78–93 (2024).
63. Kingsmore, K. M. et al. MRI analysis to map interstitial flow in the brain tumor microenvironment. *APL Bioeng*. https://doi.org/10.1063/1.5023503 (2018).
64. Lee, K., Saetern, O. C., Nguyen, A., Rodriguez, L. & Schüle, B. Derivation of leptomeninges explant cultures from postmortem human brain donors. *J. Vis. Exp.* **2017**, 55045 (2017).
65. Stirling, D. R. et al. CellProfiler 4: improvements in speed, utility and usability. *BMC Bioinformat.* **22**, https://doi.org/10.1186/s12859-021-04344-9 (2021).
66. Roberts, L. M. et al. Demonstration of chemotherapeutic-mediated changes in meningeal lymphatics in vitro, ex vivo, and in vivo [data set]. Figshare https://doi.org/10.6084/m9.figshare.c.7939814 (2025).

Acknowledgements

National Institute on Aging grant R01AG071661 and R21AG086857, National Cancer Institute R37CA222563, CCR grant from Susan G Komen CCR17483602 and National Cancer Institute 1R01CA253285 and 1R01CA262634, with aid from Grant #IRG 81-001-26 from the American Cancer Society. TF was supported by a trainee fellowship from the University of Virginia Comprehensive Cancer Center. JH was supported by the Virginia Tech Institute for Critical and Applied Science (ICTAS). Biorender was used to create schematics represented within the manuscript with licenses as follows: Fig. 1: Munson, J. (2025) https://BioRender.com/039n66o; Fig. 3A: Munson, J. (2025) https://BioRender.com/gbm2g47; Fig. 4A: Roberts, M. (2025) https://BioRender.com/ud7sa8h; Fig. 5A: Munson, J. (2025) https://BioRender.com/pv5n7rb

Author contributions

L.M.R., J.H.H., M.R.R., P.J., and J.M.M. contributed to the conceptualization, methodology, preparation, and editing of the manuscript. F.A., T.F., and M.R. conducted in vivo tumor implantation and chemotherapeutic treatment. L.M.R., F.A., T.F., and M.R. harvested tissues from vivo studies. L.M.R. performed meningeal layer dissection, tissue processing, staining, and imaging for in vivo and ex vivo studies and analysis. J.H.H. developed the in vitro tissue-engineered model and performed staining, imaging, and analysis. J.J.C. developed the Cellprofiler pipeline for diameter quantification for meningeal layers. P.J. and S.D. performed in vivo chemotherapeutic treatments in tumor-naïve in vivo studies. P.J. performed behavioral testing in chemotherapeutic treated in vivo tumor naïve studies. L.M.R. harvested tissues from tumor-naïve studies. S.D. and M.W. performed magnetic resonance imaging in chemotherapeutic-treated tumor naïve in vivo studies. J.J.C. and S.S. developed the pipeline for magnetic resonance imaging analysis.

Competing interests

The authors declare no competing interests.

Additional information

Supplementary information The online version contains supplementary material available at https://doi.org/10.1038/s42003-025-08784-4.

Correspondence and requests for materials should be addressed to L. Monet Roberts or Jennifer Munson.

Peer review information *Communications Biology* thanks the anonymous reviewers for their contribution to the peer review of this work. Primary handling editor: Christina Karlsson Rosenthal. A peer review file is available.

Reprints and permissions information is available at http://www.nature.com/reprints

Publisher's note Springer Nature remains neutral with regard to jurisdictional claims in published maps and institutional affiliations.

Open Access This article is licensed under a Creative Commons Attribution-NonCommercial-NoDerivatives 4.0 International License, which permits any non-commercial use, sharing, distribution and reproduction in any medium or format, as long as you give appropriate credit to the original author(s) and the source, provide a link to the Creative Commons licence, and indicate if you modified the licensed material. You do not have permission under this licence to share adapted material derived from this article or parts of it. The images or other third party material in this article are included in the article's Creative Commons licence, unless indicated otherwise in a credit line to the material. If material is not included in the article's Creative Commons licence and your intended use is not permitted by statutory regulation or exceeds the permitted use, you will need to obtain permission directly from the copyright holder. To view a copy of this licence, visit http://creativecommons.org/licenses/by-nc-nd/4.0/.

© The Author(s) 2025